



# Research on the Particle Breakage of Rockfill Materials during Triaxial Tests

Yufeng Jia<sup>1</sup>; Bin Xu<sup>2</sup>; Shichun Chi<sup>3</sup>; Biao Xiang<sup>4</sup>; and Yang Zhou<sup>5</sup>

**Abstract:** Particle breakage modifies a rockfill structure, influencing its dilatancy, friction angle, strength, and permeability, as well as generating creep deformation, wetting deformation, and residual strain under a seismic load. However, the breakage laws of rockfill during shearing remain unclear. This paper investigates the particle breakage of the basalt rockfill that is used in the Gushui concrete face rockfill dam during specimen preparation, consolidation, and drained triaxial shearing. The results indicate that the hammer compaction during specimen preparation generates a considerable amount of particle breakage, whereas isotropic consolidation generates negligible particle breakage. Under a low confining pressure (100 kPa), rockfill particle sliding and roll over are loosely constrained, and negligible particle breakage occurs during triaxial shearing. Under a high confining pressure (greater than 500 kPa), rockfill particle sliding and roll over are more constrained. Thus, the contact force significantly increases and significant particle breakage occurs. During triaxial shearing, larger diameter particles break first and smaller diameter particles begin to break as the confining pressure increases. The percentage of particles with diameters below 0.25 mm always increases with increasing shearing strain, and the amplitude increases with increasing confining pressure. Particle breakage during shearing in the triaxial test is affected by both the shear strain and stress. Additionally, the relationship between the relative particle breakage index and plastic work can be simulated with a hyperbolic formulation. DOI: [10.1061/\(ASCE\)GM.1943-5622.0000977](https://doi.org/10.1061/(ASCE)GM.1943-5622.0000977). © 2017 American Society of Civil Engineers.

**Author keywords:** Particle breakage; Rockfill; Consolidate drained triaxial test; Relative particle breakage index.

## Introduction

### *Influence of Particle Breakage on the Rockfill Material's Constitutive Characteristics*

Earth-rockfill dams are the most widely used dams in hydropower engineering because of their facile material selection, low cost, simple structure, and adaptability to topography and geology (Xiao et al. 2016d; Zhang et al. 2012). Over the last two decades, many earth-rockfill dams with heights greater than 200 m and even reaching 300 m have been constructed or are under construction (Wu et al. 2016). With these increases in dam height, the rockfill, which is the main material used in dam engineering, is subjected to significant stress. Therefore, the particle breakage of rockfill in high earth-rockfill dams significantly increases. This particle breakage directly modifies the rockfill structure, influencing its

dilatancy, friction angle, strength, and permeability, as well as generating creep deformation, wetting deformation, and residual strain under a seismic load (Indraratna et al. 2010, 2012, 2014; Kong et al. 2016; Xiao et al. 2016d; Zhang et al. 2015). Over the last half-century, numerous laboratory tests have been performed to research rockfill particle breakage, and, specifically, to investigate the relationship between particle breakage and strength (Marachi et al. 1972; Marsal 1967; McDowell and Bolton 1998; Varadarajan et al. 2006; Xiao et al. 2014, 2015, 2016a, b, c; Xiao and Liu 2017), stress paths (Hardin 1985; Yang et al. 2010), cyclic loading (Indraratna et al. 2012, 2013; Sun et al. 2014), creep deformation (McDowell 2003; Oldecop and Alonso 2001), wetting deformation (Chavez and Alonso 2003; Zhang et al. 2015), and energy (Indraratna and Salim 2002; Jia et al. 2009; Xiao et al. 2014).

### *Limitations of Particle Breakage Research*

During rockfill deformation, the work performed by loading is consumed by friction among the particles and the particles' roll over, breakage, and restructuring. The rockfill's constitutive characteristics are controlled by the particles' friction, roll over, breakage, and rearrangement. During these processes, particle breakage changes the contact status among particles, affecting the particle friction, reducing the particle roll over, and causing particle restructuring. Thus, particle breakage is a key factor that controls rockfill deformation, especially in high earth-rockfill dams. The creep deformation generated by rockfill particle breakage caused the Tianshengqiao No. 1 concrete face rockfill dam (CFRD) in China, which has a height of 175 m, to undergo a maximum settlement of 100 cm within 1 year after completion. Thus, 52% of the concrete face separated from the cushion zone, with a maximum separation distance of 15 cm (Ma and Cao 2007). The plastic deformation of the rockfill generated by particle breakage and restructuring after the Wenchuan earthquake caused the Zipingpu CFRD in China to undergo a maximum settlement of 810.3 mm, and the maximum horizontal displacement exceeded 300 mm (Kong et al.

<sup>1</sup>Lecturer, State Key Laboratory of Coastal and Offshore Engineering, School of Hydraulic Engineering, Dalian Univ. of Technology, Dalian, Liaoning 116024, China.

<sup>2</sup>Associate Professor, State Key Laboratory of Coastal and Offshore Engineering, School of Hydraulic Engineering, Dalian Univ. of Technology, Dalian, Liaoning 116024, China.

<sup>3</sup>Professor, State Key Laboratory of Coastal and Offshore Engineering, School of Hydraulic Engineering, Dalian Univ. of Technology, Dalian, Liaoning 116024, China (corresponding author). E-mail: 39492153@qq.com

<sup>4</sup>Engineer, POWERCHINA Kunming Engineering Corporation, Kunming, Yunnan 650000, China.

<sup>5</sup>Engineer, State Key Laboratory of Coastal and Offshore Engineering, School of Hydraulic Engineering, Dalian Univ. of Technology, Dalian, Liaoning 116024, China.

Note. This manuscript was submitted on October 27, 2016; approved on April 24, 2017; published online on July 25, 2017. Discussion period open until December 25, 2017; separate discussions must be submitted for individual papers. This paper is part of the *International Journal of Geomechanics*, © ASCE, ISSN 1532-3641.

2010). The laws of rockfill particle breakage during deformation under loading provide the basis for studying the mechanisms of structural changes and energy conversion associated with rockfill deformation. Additionally, these laws can be used to study the relationship between the macro properties of the soil and changes in the microstructure (Jensen et al. 2001; Li et al. 2016; Lobo-Guerrero et al. 2006). However, previous studies primarily focused on the amount of particle breakage before and after the tests, so the rockfill particle breakage during these tests was poorly understood. Indraratna and Salim (2002) conducted a series of large-scale triaxial tests to study the particle breakage of latite basalt rockfill during shearing. However, the maximum confining pressure of these tests was only 300 kPa, which is considerably less than the actual confining pressures in high earth-rockfill dams. Zhang et al. (2014) studied the particle breakage of a simulated rockfill during shearing by using a medium-scale triaxial test. However, the simulated rockfill consisted of cement ellipsoid aggregate and was less angular than actual rockfill. Thus, the simulated rockfill density was lower, and less interlocking was present among these particles than in actual rockfill.

### Particle Breakage of Rockfill Materials during Triaxial Tests

In this study, a series of large-scale, consolidated drained (CD) triaxial tests was performed by using the Gushui rockfill to investigate its particle breakage at certain shearing strains during triaxial tests under different confining pressures. The relationships among the particle breakage and the shear strain, confining pressure, shear stress, and plastic work were analyzed. The objective of this paper is to investigate the particle breakage laws of the rockfill material during shearing in CD triaxial compression tests. The research used in this paper will provide valuable information regarding the relationship between the constitutive characteristics of the rockfill and changes in the microstructure.

### Testing Apparatus and Material

The triaxial compression test was conducted by using a large-scale multifunctional triaxial apparatus developed by the Dalian University of Technology in China. The apparatus can accommodate specimens with diameters of 300 mm and heights of 600 mm.

A schematic view of the device is shown in Fig. 1. The largest axial load is 1,500 kN (6 MPa), and the largest confining pressure is 3 MPa, both of which can be applied by controlling either the displacement or force. The volumetric strain of the specimen is obtained by measuring the outgoing or incoming water volume of the specimen by using a high-precision scale sensor.

The rockfill used in the test was moderately weathered basalt from the Gushui quarry in Yunnan Province, China. The basalt rockfill was mined from the quarry by blasting and crushed in situ using the stonebreaker and sieved according to the grain distribution. The basalt rockfill had a specific gravity of 2.79, the maximum water absorption rate was 0.3%, the average length-diameter ratio of the rockfill particles was 1.76, and the compressive strength of the parent rock was 83.5 MPa. The maximum rockfill particle diameter of the design gradation was 800 mm. According to Chinese Standard SL237-1999 (CS 1999), which requires the ratio of the specimen diameter to the maximum particle diameter in tests to be 5, the maximum particle diameter of the specimens was 60 mm ( $=300/5$ ). Thus, the design gradation of the rockfill was scaled to the test gradation by using a mixed method according to CS SL237-1999 (CS 1999). Fig. 2 shows the design gradation and test gradation of the rockfill. The dry density of the specimen was  $2.21 \text{ g/cm}^3$ , and the initial void ratio was 0.262.

### Test Program and Test Procedures

Gao et al. (2009) found that particle breakage appears during the preparation of rockfill specimens. To accurately measure the rockfill particle breakage that occurs during specimen prep-

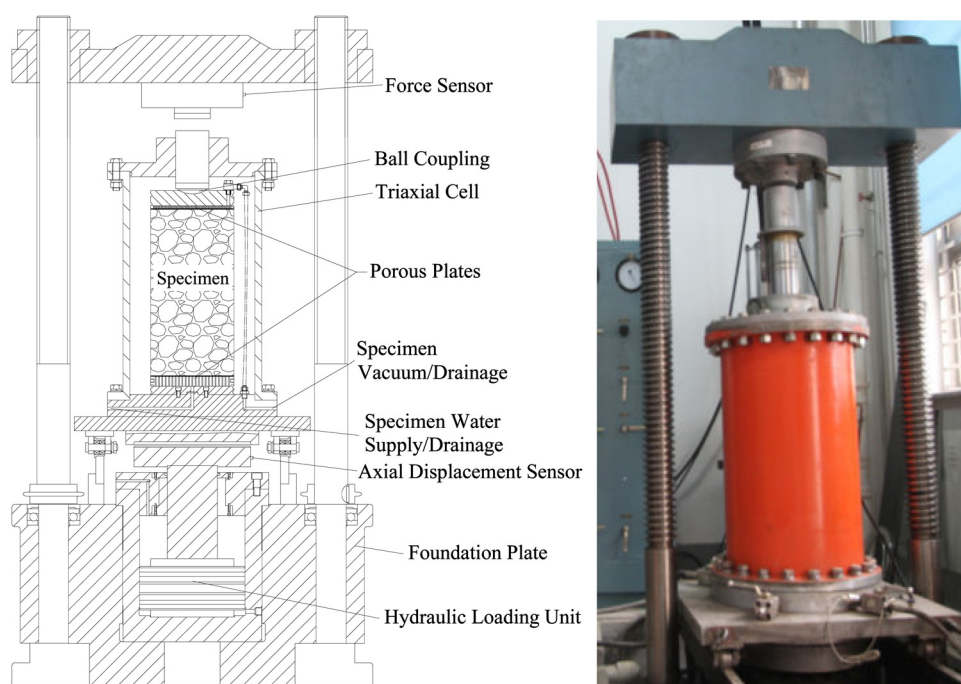


Fig. 1. (Color) Schematic view of the large triaxial apparatus

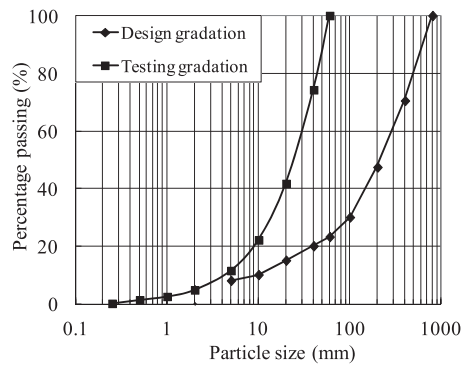


Fig. 2. Rockfill gradation used in the tests

aration, consolidation, and triaxial shearing, three types of tests were performed on the rockfill under different conditions: a specimen preparation test, consolidation tests, and CD triaxial compression tests.

### Specimen Preparation Test

The specimen was compacted inside a 5-mm-thick rubber membrane in a split cylindrical mold. The rockfill was mixed and compacted in six layers by using a vibratory hammer at a dry density of  $2.21 \text{ g/cm}^3$ . The specimen was dried and sieved after compaction, and the particle breakage generated by the specimen's compaction was obtained.

### Consolidation Tests

A new specimen was prepared according to the method described in the previous section by using new rockfill. After compaction, any punctures in the rubber membrane generated by the rockfill were repaired. The stress and volumetric strain measurements were corrected for the membrane penetration, as described by Yang et al. (2010). The specimen was placed in the triaxial cell and saturated under a confining pressure of 30 kPa.  $\text{CO}_2$  was then introduced from the bottom plate to replace the air in the specimen before specimen saturation. The specimen was isotropically consolidated after the saturation reached 95%. During consolidation, the water was drained from the plates at the bottom and top of the specimen. After the drained water had stabilized, the confining pressure was unloaded. The specimen was dried and sieved after consolidation and the amount of particle breakage generated by specimen compaction and isotropic consolidation was obtained. Two consolidated tests were completed at confining pressures of 500 and 1,500 kPa.

### CD Triaxial Compression Tests

A new specimen was prepared and consolidated according to the methods in the previous two sections by using new rockfill. After consolidation, the specimen was sheared to a given shear strain at an axial strain rate of 0.5 mm/min (0.1%/min). Fig. 3 shows the stress-strain curves at various shear strains under a confining pressure of 2,000 kPa.

Table 1 lists the unloading shearing strains at confining pressures of 100, 500, 1,000, 1,500, and 2,000 kPa. After the shear strain reached these unloading shear strains, the specimen was unloaded, dried, and sieved, and the particle breakage was obtained at various shear strains. Thus, the rockfill particle breakage during triaxial shearing was measured according to the results of the consolidation tests and CD triaxial compression tests.

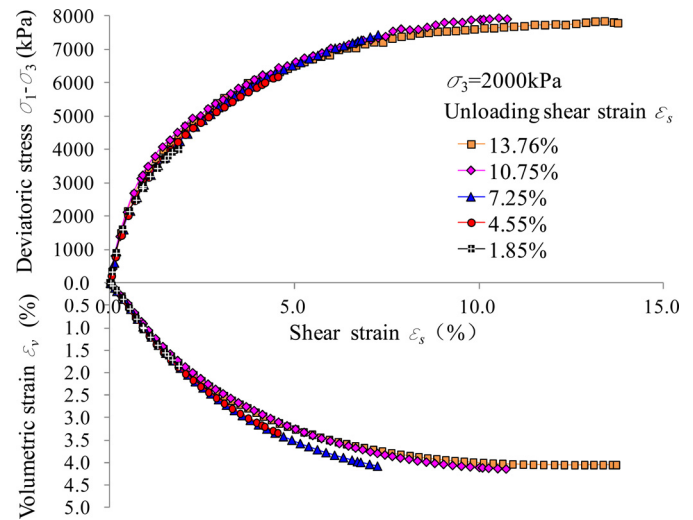


Fig. 3. (Color) Stress-strain curves at a confining pressure of 2,000 kPa

Table 1. Unloading Shear Strains under Various Confining Stresses

$\sigma_3$ (kPa)	Unloading shear strain $\epsilon_s$ (%)				
	First	Second	Third	Fourth	Fifth
100	0.58 <sup>a</sup>	4.41 <sup>b</sup>	8.57	11.12	18.46
500	1.87 <sup>a</sup>	4.56	8.44 <sup>b</sup>	12.49	16.01
1,000	1.75	4.60	7.20 <sup>a</sup>	10.66 <sup>b</sup>	15.19
1,500	1.90	7.34	9.39 <sup>a</sup>	12.47 <sup>b</sup>	14.35
2,000	1.85	4.55	7.25	10.75	13.76

<sup>a</sup>Maximum volumetric strain occurred.

<sup>b</sup>Peak shear strength occurred.

### Test Results

#### Particle Breakage during the Specimen Preparation and Consolidation Tests

Table 2 lists the rockfill gradation levels before and after the specimen preparation and consolidation tests. Table 2 shows that the rockfill gradation considerably changed after specimen preparation. Fig. 4 shows the gradation curves before the test, after specimen preparation, and after isotropic consolidation.

Table 2 and Fig. 4 illustrate that the rockfill gradations after isotropic consolidation at 500 and 1,500 kPa did not notably differ from the rockfill gradation after specimen preparation. This result indicates that the particle breakage generated by hammer compaction during specimen preparation could not be ignored and that isotropic consolidation generated negligible particle breakage. Thus, the gradation after specimen preparation was directly used as the initial gradation to measure the amount of particle breakage during the triaxial tests.

#### Particle Breakage in the CD Triaxial Shearing Tests

The stress-strain curves under the various confining pressures are shown in Fig. 5. The largest shear strains at confining pressures of 100, 500, 1,000, 1,500, and 2,000 kPa were 13.76, 14.35, 15.19, 16.01, and 18.46%, respectively; these shear strains were affected by the volumetric strain.



**Table 2.** Rockfill Gradation after Sample Preparation and Consolidation

Status	$\sigma_3$ (kPa)	Particle quantity (%) in each grain group (mm)										
		40–60	20–40	10–20	5–10	2–5	1–2	0.5–1	0.25–0.5	0.1–0.25	0.075–0.1	<0.075
Before the test	—	25.77	32.59	19.60	10.65	6.71	2.29	1.17	1.22	—	—	—
After specimen preparation	—	18.39	36.19	19.51	11.33	8.13	1.92	2.15	1.20	0.41	0.13	0.64
After consolidation	500	19.46	34.85	20.74	10.53	8.02	1.71	2.25	1.25	0.38	0.13	0.68
	1,500	19.04	36.03	18.18	13.82	6.78	1.60	2.31	1.19	0.44	0.13	0.48

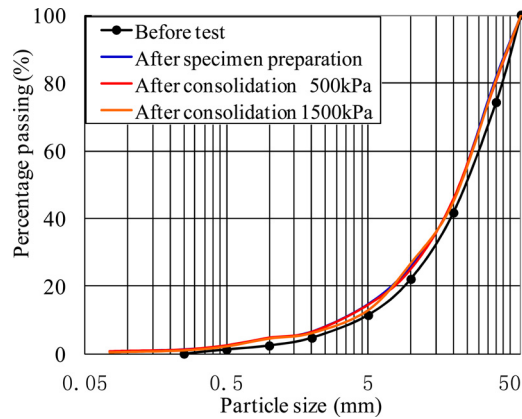
**Fig. 4.** (Color) Rockfill gradation curves before and after the tests

Fig. 5 demonstrates the convergence of the  $(\sigma_1 - \sigma_3) \sim \varepsilon_s$  and  $\varepsilon_v \sim \varepsilon_s$  curves at various terminal shear strains under the same confining pressure, which indicates that these tests exhibited good repeatability under the same confining pressure. Additionally, the stress-strain relationships of the specimens at various terminal shear strains were consistent, and the specimens at the same confining pressure could be regarded as one specimen. Thus, the soil gradations of the specimens at various terminal shear strains under the same confining pressure could be regarded as the soil gradations of one specimen, as listed in Table 3.

Table 3 shows that the changes in rockfill gradation at every shear strain under a confining pressure of 100 kPa were negligible compared with the rockfill gradation after specimen preparation. Fig. 5 shows that the  $(\sigma_1 - \sigma_3) \sim \varepsilon_s$  curves under a confining pressure of 100 kPa exhibited a clear strain-softening region, and the  $\varepsilon_v \sim \varepsilon_s$  curves exhibited significant dilatancy. This result indicates that the confining pressure of 100 kPa could not limit rockfill particle sliding and roll over, and little particle breakage occurred during the triaxial shearing. The deviator stress of the rockfill under a confining pressure of 100 kPa was mainly generated by the sliding friction and dilatancy.

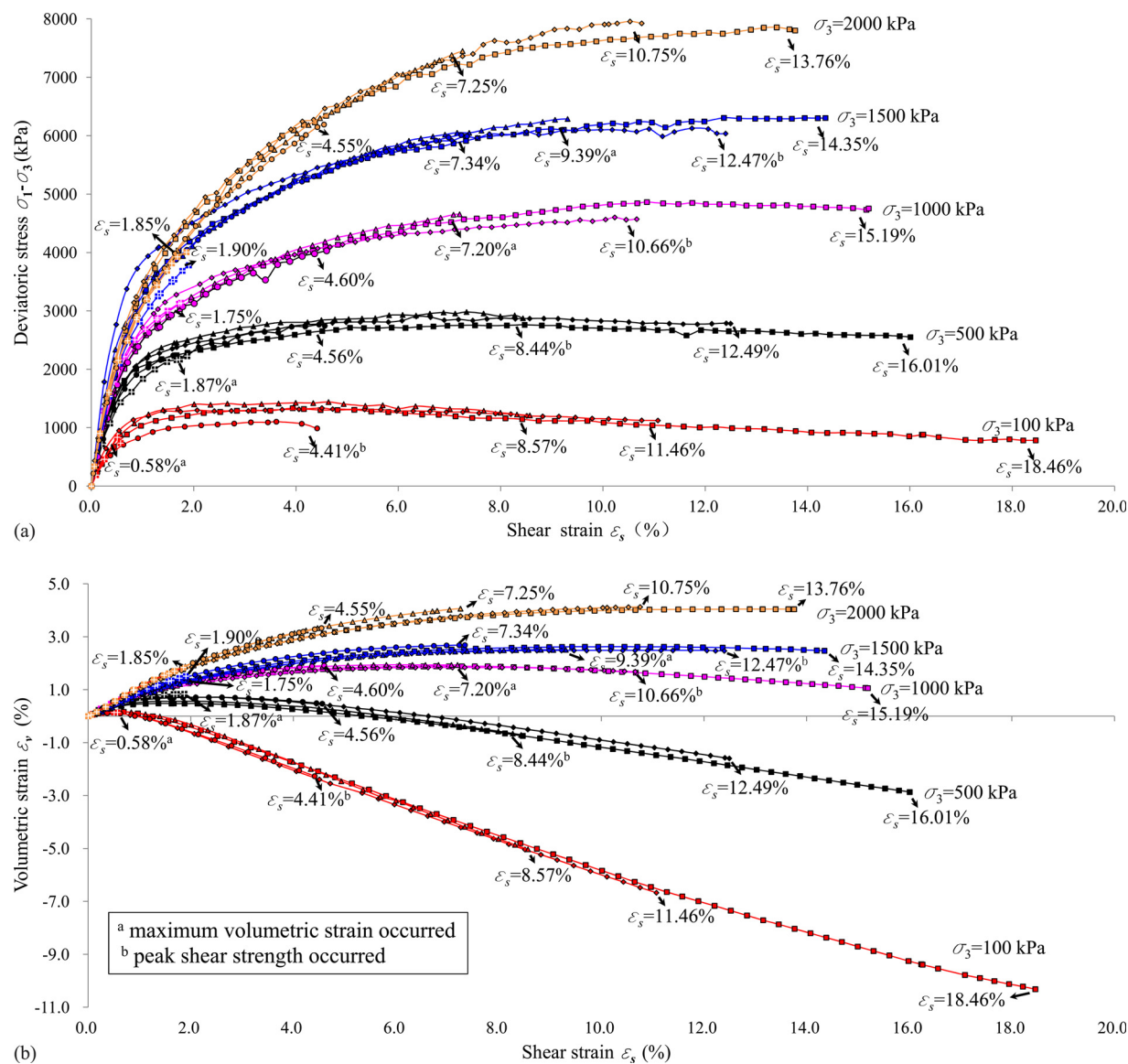
As shown in Table 3, significant particle breakage occurred as the confining pressure increased to 500 kPa. Fig. 6 shows the granularity distribution curves at every terminal shear strain at 500 kPa. Table 3 and Fig. 6 illustrate that when the shear strain increased from 1.87 to 16.01%, the percentage of particles with diameters of 40–60 mm decreased from 18.91 to 11.27%, the percentage of particles with diameters of 20–40 mm increased from 35.46 to 37.97%, the percentage of particles with diameters of 0.075–0.1 mm increased from 0.14 to 0.22%, and the percentage of particles with diameters under 0.075 mm increased from 0.78 to 1.14%. The percentage of particles with diameters of 0.25–20 mm did not exhibit a clear trend during the triaxial tests.

Fig. 5 shows that the  $(\sigma_1 - \sigma_3) \sim \varepsilon_s$  curves under a confining pressure of 500 kPa displayed a slight strain-softening region,

and the dilatancy of the  $\varepsilon_v \sim \varepsilon_s$  curves significantly decreased. This result indicates that the confining pressure of 500 kPa exhibited a tight constraint, and the particles with diameters of 40–60 mm could not freely roll over; thus, the contact force among the particles increased. This higher contact force generated particle breakage and increased the shear strength of the rockfill, significantly decreasing the dilatancy. However, the increase in the percentage of particles with diameters of 20–40 mm indicates that the higher contact force could not effectively break these particles, and some particles with diameters of 40–60 mm subjected to angular fracturing (Zhang et al. 2012) became particles with diameters of 20–40 mm. The increase in the percentage of particles with diameters under 0.1 mm exceeded 50%, indicating that the higher confining pressure increased the rockfill compactness and thus the amount of particle contact, which in turn increased the degree of particle abrasion (Cooper and Breau 2010) during particle sliding and roll over.

Fig. 7 shows the broken particles under confining pressures of 2,000 and 500 kPa. Particles within the same grain group had the same mass. Fig. 7 shows that the broken particles at a shear strain of 1.87% under a confining pressure of 500 kPa were the most angular, which was very similar to the initial sample. The broken particles at a shear strain of 13.76% under a confining pressure of 2,000 kPa were the most round. The broken particles at a shear strain of 16.01% under a 500-kPa confining pressure and the particles at a shear strain of 1.85% under a 2,000-kPa confining pressure were in the middle, which illustrates that the particle angularity decreased with increasing confining pressure and shear strain. The higher confining pressure and larger shear strain generated more particle abrasion and increased the percentage of particles with diameters under 0.25 mm. Furthermore, the particle abrasion and angular fracturing of particles with diameters of 20–60 mm increased the percentage of particles with diameters of 0.25–20 mm. However, the particle breakage of particles with diameters of 0.25–20 mm decreased the percentage of particles with this range of diameters. The growth and decline of these two influencing factors resulted in no clear variations in the percentage of particles with diameters of 0.25–20 mm in the triaxial tests.

Fig. 8 shows the percentages of particles with diameters of 40–60 mm, 20–40 mm, and under 0.25 mm in the triaxial tests at confining pressures of 500, 1,000, 1,500, and 2,000 kPa. The percentage of particles with diameters of 40–60 mm decreased with increasing shear strain at every confining pressure, and the percentage of particles with diameters of 20–40 mm under a confining pressure of 500 kPa increased with increasing shear strain. The percentage of particles with diameters of 20–40 mm under a confining pressure of 1,000 kPa increased from 34.25 to 36.74% with an increase in the shear strain from 1.75 to 7.20%, and the percentage then decreased to 33.05% with a further increase in the shear strain to 15.19%. Additionally, the percentage of particles with diameters of 20–40 mm under confining pressures of 1,500 and 2,000 kPa decreased with increasing shear strain. The percentage of particles with diameters under 0.25 mm increased with increasing shear



**Fig. 5.** (Color) Stress-strain curves under the different shear strains during the triaxial tests: (a) deviatoric stress and shear strain curves; (b) volumetric strain and shear strain curves

strain at every confining pressure, and the amplitude increased with increasing confining pressure.

Fig. 5 shows that the  $(\sigma_1 - \sigma_3) \sim \varepsilon_s$  curves under a confining pressure of 1,000 kPa also displayed a slight strain-softening region, and the dilatancy of the  $\varepsilon_v \sim \varepsilon_s$  curves was less than 500 kPa. A comparison of the variation in the particle amounts and the stress-strain curves under confining pressures of 500 and 1,000 kPa indicates that the confining pressure of 1,000 kPa was sufficiently large to limit particles with diameters of 20–40 mm from rolling over. Additionally, the contact force between the particles increased, causing more particles with diameters of 20–40 mm to break during shearing. However, at the beginning of shearing, particles with diameters of 40–60 mm broke first, and a portion of these particles subjected to angular fracturing became particles with diameters of 20–40 mm. Thus, the percentage of particles with diameters of 20–40 mm increased with increasing shear strain at the beginning of shearing, and the percentage of particles reached a maximum of 36.74% at a shear strain of 7.20%, at which the maximum volumetric compression occurred and dilatancy began.

Fig. 5 shows that the strain softening of the  $(\sigma_1 - \sigma_3) \sim \varepsilon_s$  curves and dilatancy of the  $\varepsilon_v \sim \varepsilon_s$  curves decreased under a confining pressure of 1,500 kPa. As the confining pressure increased to 2,000 kPa, the  $(\sigma_1 - \sigma_3) \sim \varepsilon_s$  curves exhibited strain hardening, and no dilatancy occurred in the  $\varepsilon_v \sim \varepsilon_s$  curves. Comparisons of the variations in the particle quantities and the stress-strain curves under confining pressures of 1,000, 1,500, and 2,000 kPa indicate that approximately half of the particles with diameters of 40–60 mm broke apart and particles with diameters of 20–40 mm experienced significant particle breakage as the confining pressure increased. The larger confining pressure and more common particle breakage further decreased and even prevented dilatancy.

### Analysis of Particle Breakage during Triaxial Shearing

The relative breakage  $B_r$  was used to measure the amount of rockfill particle breakage. Hardin (1985) defined the breakage potential  $B_p$  as the area between the grain-size distribution curve of the soil and the 0.074-mm line, as shown in Fig. 9.

**Table 3.** Rockfill Gradation at Various Shear Strains during the Triaxial Tests

Status		$\varepsilon_s$ (%)	Particle quantity (%) in each grain group (mm)										
			40–60	20–40	10–20	5–10	2–5	1–2	0.5–1	0.25–0.5	0.1–0.25	0.075–0.1	<0.075
After specimen preparation			18.39	36.19	19.51	11.33	8.13	1.92	2.15	1.20	0.41	0.13	0.64
$\sigma_3$ (kPa)	100	0.58 <sup>a</sup>	20.39	33.99	20.17	12.26	7.15	1.92	1.96	1.12	0.36	0.11	0.57
		4.41 <sup>b</sup>	17.58	36.86	19.28	12.55	7.16	1.92	2.11	1.23	0.42	0.13	0.76
		8.57	17.90	36.28	19.08	11.20	8.31	2.10	2.44	1.31	0.48	0.14	0.77
		11.12	18.44	34.15	20.10	12.44	7.67	2.14	2.37	1.31	0.45	0.13	0.80
		18.46	17.37	36.45	18.49	13.04	7.48	2.03	2.39	1.32	0.46	0.15	0.82
	500	1.87 <sup>a</sup>	18.91	35.46	19.39	11.91	7.48	1.87	2.37	1.25	0.46	0.14	0.78
		4.56	15.78	35.81	21.08	12.55	7.84	1.93	2.42	1.30	0.42	0.12	0.74
		8.44 <sup>b</sup>	14.18	35.02	21.05	13.75	8.31	1.95	2.66	1.46	0.50	0.17	0.94
		12.49	14.99	35.86	19.32	12.74	9.21	2.10	2.76	1.54	0.50	0.15	0.83
		16.01	11.27	37.97	21.80	13.62	8.18	1.53	2.50	1.38	0.41	0.22	1.14
	1,000	1.75	18.76	34.25	19.51	12.97	7.88	1.95	2.27	1.26	0.39	0.13	0.62
		4.60	14.78	35.87	20.08	13.33	8.62	1.92	2.66	1.40	0.47	0.15	0.73
		7.20 <sup>a</sup>	11.82	36.74	20.11	13.37	9.73	2.08	2.94	1.58	0.54	0.17	0.91
		10.66 <sup>b</sup>	12.46	34.43	26.00	10.26	8.81	2.15	2.71	1.53	0.53	0.18	0.95
		15.19	11.59	33.05	21.59	15.11	8.91	1.86	3.58	1.90	0.79	0.26	1.36
	1,500	1.90	17.47	35.96	18.86	11.93	8.74	1.98	2.41	1.34	0.43	0.14	0.74
		7.34	11.59	34.46	20.57	14.21	10.26	2.06	3.30	1.74	0.63	0.21	0.96
		9.31 <sup>a</sup>	12.24	33.54	21.07	14.35	9.45	1.96	3.39	1.81	0.74	0.24	1.22
		12.47 <sup>b</sup>	10.44	32.86	21.58	14.97	10.28	2.42	3.19	1.87	0.74	0.24	1.42
		14.35	9.42	32.18	22.13	15.84	10.17	2.20	3.37	1.98	0.84	0.24	1.62
	2,000	1.85	16.54	36.69	19.20	12.60	7.82	2.03	2.30	1.27	0.48	0.15	0.93
		4.55	14.90	34.97	19.06	13.19	9.34	2.11	2.98	1.58	0.58	0.19	1.10
		7.26	12.00	34.35	20.23	13.66	10.08	2.47	3.08	1.67	0.70	0.21	1.23
		10.75	9.38	34.66	20.63	14.31	10.61	2.46	3.57	1.85	0.77	0.24	1.52
		13.76	9.78	34.22	19.32	14.51	10.45	2.54	4.03	2.12	0.91	0.29	1.81

<sup>a</sup>Maximum volumetric compression occurred.<sup>b</sup>Peak shear strength occurred.

The change in the  $B_p$  value of the soil before and after the test was defined as the total breakage  $B_t$ , as shown in Fig. 9. Hardin then defined the relative breakage,  $B_r$ , as the total breakage divided by the potential breakage ( $B_t/B_p$ ). Hardin developed the relationship between  $B_r$  and stress according to triaxial test results of rockfill

$$B_r = \frac{\left(\frac{\sigma_b}{\sigma_r}\right)^{n_b}}{1 + \left(\frac{\sigma_b}{\sigma_r}\right)^{n_b}} \quad (1a)$$

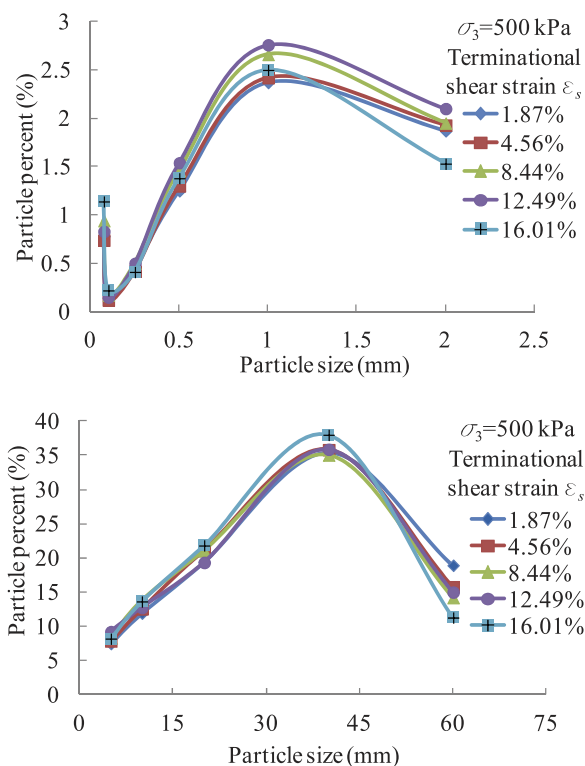
$$\sigma_b = \sigma_0 \left[ 1 + 9 \left( \frac{\tau_0}{\sigma_0} \right)^3 \right] \quad (1b)$$

$$\sigma_r = 800P_a(n_b - 0.3) \quad (1c)$$

$$n_b = \frac{h^2}{(1 + e_i)n_s} + 0.3 \quad (1d)$$

where  $\sigma_b$  = breakage effective stress;  $\sigma_r$  = breakage reference stress;  $n_b$  = breakage number;  $\sigma_0$  and  $\tau_0$  = effective octahedral normal and shear stresses, respectively;  $P_a$  = atmospheric pressure;  $e_i$  = initial void ratio;  $h$  = scratch hardness; and  $n_s$  = shape number.

Table 4 lists the relative breakage index  $B_r$ , which was calculated according to the rockfill gradation list in Table 3, at various shear

**Fig. 6.** (Color) Granularity distribution curves at various shear strains at 500 kPa

strains during the triaxial tests at confining pressures of 500, 1,000, 1,500, and 2,000 kPa. The corresponding volumetric strains  $\varepsilon_v$  and maximum shear stresses  $(\sigma_1 - \sigma_3)_{\max}$  are also listed in Table 4;  $(\sigma_1 - \sigma_3)_{\max}$  is the maximum  $(\sigma_1 - \sigma_3)$  observed before unloading. The  $B_r$  values listed in Table 4 eliminated the particle breakage during specimen preparation.

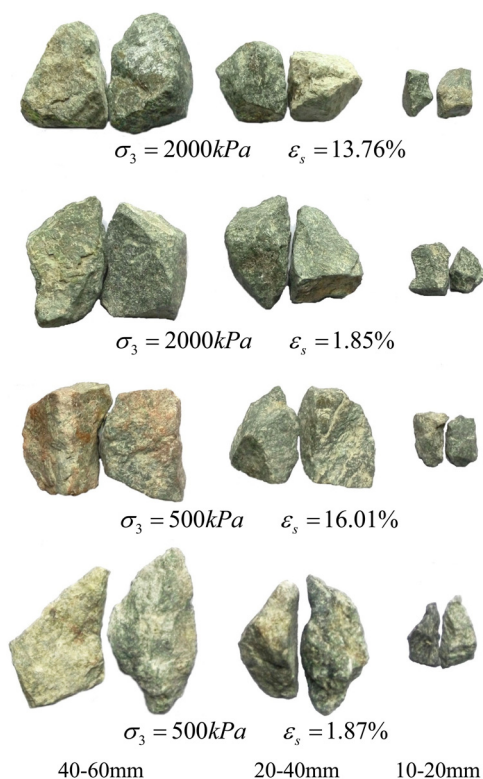


**Fig. 7.** (Color) Particles subject to breakage

Table 4 shows that as  $\varepsilon_s$  increased from 1.87 to 16.01% at a confining pressure of 500 kPa, the corresponding  $\varepsilon_v$  decreased from 0.85 to  $-2.87\%$ , and the corresponding  $B_r$  increased from 0.19 to 2.41%. As  $\varepsilon_s$  increased from 7.20 to 15.19% at a confining pressure of 1,000 kPa, the corresponding  $\varepsilon_v$  decreased from 1.94 to 1.06%, and the corresponding  $B_r$  increased from 3.29 to 4.98%. This result indicates that significant particle breakage was generated in the rockfill, even when the specimen was completely in the dilatancy stage. Additionally, at the same confining pressure  $\sigma_3$ , the shear strain  $\varepsilon_s$  had a larger influence on the volumetric strain  $\varepsilon_v$  than the particle breakage. The same phenomenon appeared in the triaxial test at a confining pressure of 1,500 kPa. Fig. 10 shows the  $\varepsilon_v$  value at a similar shear strain  $\varepsilon_s$ , which excluded the influence of  $\varepsilon_s$ , under confining pressures of 1,500 and 2,000 kPa. Fig. 10 shows that the  $B_r$  value under confining pressures of 1,500 and 2,000 kPa exhibited an almost 500% increase, but the  $\varepsilon_v$  value under confining pressures of 1,500 and 2,000 kPa exhibited a 178 and 221% increase, respectively. This result indicates that the confining pressure  $\sigma_3$  had a larger influence on the volumetric strain  $\varepsilon_v$  than the particle breakage.

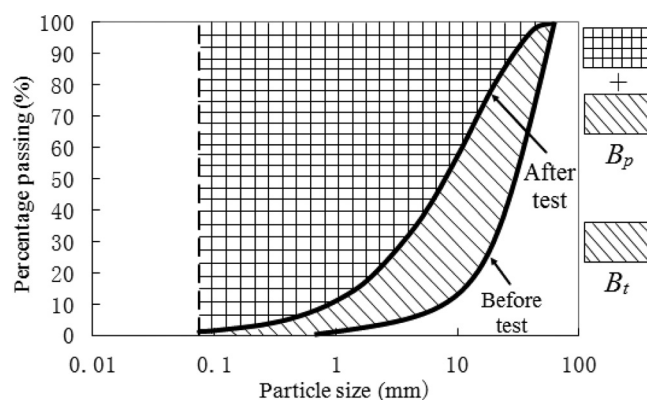


**Fig. 9.** Definition of the relative breakage index

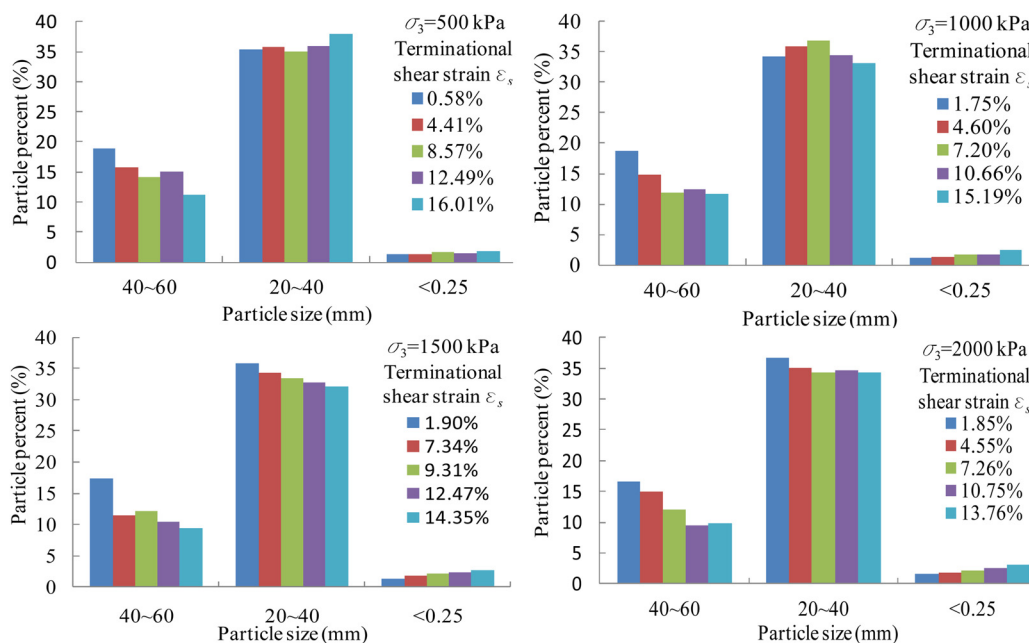


**Fig. 8.** (Color) Variations in the percentages of particles during the triaxial tests



**Table 4.**  $B_r$  during Triaxial Tests

Status ( $\sigma_3$ /kPa)	$\varepsilon_s$ (%)	$\varepsilon_v$ (%)	$(\sigma_1 - \sigma_3)_{\max}$ (kPa)	$B_r$ (%)	$B_r^*$ (%) <sup>a</sup>
500	1.87	0.85	2,226	0.19	0.09
	4.56	0.47	2,766	1.05	1.58
	8.44	-0.71	2,982	2.34	2.39
	12.49	-1.60	2,906	2.21	2.10
	16.01	-2.87	2,761	2.41	1.56
1,000	1.75	1.24	3,139	0.39	0.32
	4.60	1.92	4,030	1.82	2.92
	7.20	1.94	4,655	3.29	5.14
	10.66	1.68	4,602	2.69	4.94
	15.19	1.06	4,864	4.98	5.94
1,500	1.90	1.51	3,782	0.88	0.56
	7.34	2.69	6,011	4.32	7.09
	9.31	2.51	6,288	4.51	8.10
	12.47	2.47	6,128	5.63	7.51
	14.35	2.47	6,306	6.39	8.17
2,000	1.85	1.84	4,007	0.96	0.20
	4.55	3.33	6,192	2.95	5.43
	7.26	4.07	7,451	4.55	9.54
	10.75	4.13	7,958	5.98	11.35
	13.76	4.04	7,856	6.85	10.98

<sup>a</sup> $B_r$  calculated using Hardin's function.

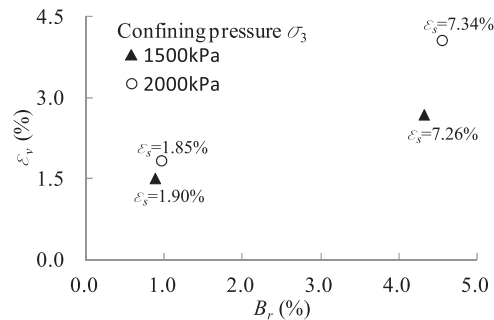
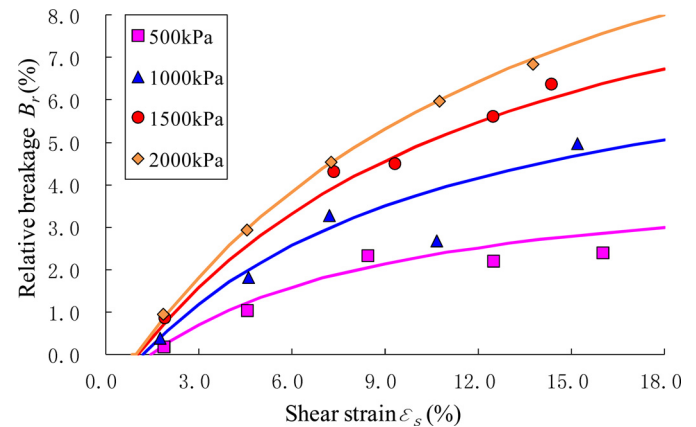
**Fig. 10.** Influence of  $s_3$  and  $B_r$  on  $e_v$ 

Table 4 shows the  $B_r$  values calculated according to Eqs. (1a)–(1d), which are marked by  $B_r^*$ . Table 4 shows that the  $(\sigma_1 - \sigma_3)_{\max}$  value at each confining pressure slightly decreased as  $\varepsilon_s$  increased, the  $B_r$  value decreased as  $(\sigma_1 - \sigma_3)_{\max}$  decreased, and the corresponding  $B_r$  at each confining pressure increased as  $\varepsilon_s$  increased. Thus, the relationship between  $B_r$  and the stress could not describe the rockfill particle breakage that occurred during the triaxial tests. This inability occurred because the preceding research focused on the particle breakage that occurred when the soil specimen reached the failure stage, in which all specimens under each confining pressure reached  $\varepsilon_1$  values of nearly 15%, and the stress's influence on particle breakage appeared to be notable. Table 5 shows that the  $B_r$  value at approximately  $\varepsilon_s$  under each confining pressure increased with increasing  $(\sigma_1 - \sigma_3)_{\max}$ , which matches the  $B_r^*$  values calculated with Eqs. (1a)–(1d). Thus,  $B_r$  at a given shear strain was mainly affected by the stress, and the shear strain and stress both affected the particle breakage during the shearing in the triaxial test.

The  $B_r$  values during the triaxial test under each confining pressure are shown in Fig. 11, which also shows that the shear strain and confining stress both affected the particle breakage. Thus, the plastic work, which reflects both the strain and stress

**Table 5.**  $B_r$  at Approximately Shear Strain under Each Confining Pressure

$\varepsilon_s$ (%)	$\sigma_3$ (per kPa)	$(\sigma_1 - \sigma_3)_{\max}$ (kPa)	$B_r$ (%)	$B_r^*$ (%)
1.87	500	2,226	0.19	0.09
1.75	1,000	3,139	0.39	0.32
1.90	1,500	3,782	0.88	0.56
1.85	2,000	4,007	0.96	0.20
4.56	500	2,766	1.05	1.58
4.60	1,000	4,030	1.82	2.92
4.55	2,000	6,192	2.95	5.43
7.20	1,000	4,655	3.29	5.14
7.34	1,500	6,011	4.32	7.09
7.26	2,000	7,451	4.55	9.54

**Fig. 11.** (Color) Relative breakage index  $B_r$  during the triaxial tests**Table 6.** Plastic Strain and  $W_p$  during the Triaxial Test at a Confining Pressure of 2,000 kPa

$\sigma_3$ (kPa)	$\varepsilon_s$ (%)	$\varepsilon_s^p$ (%)	$\varepsilon_v^p$ (%)	$W_p$ (kJ/m <sup>3</sup> )
2,000	1.85	1.57	1.86	91.1
	4.55	4.11	3.40	288.8
	7.26	6.71	4.23	511.8
	10.75	10.11	4.40	800.3
	13.76	13.14	4.30	1017.6

during shearing, can be used to simulate the particle breakage during shearing.

### Particle Breakage from Plastic Work

Particle breakage is a process in which the work performed by the load is transformed into the surface energy of the new broken particles (Griffith 1921). Many researchers have related particle breakage to energy, by which the particle breakage was incorporated into a constitutive soil model (Liu et al. 2014; McDowell and Bolton 1998; Salim and Indraratna 2004). Thus, the plastic work  $W_p$  that corresponds to  $B_r$  in the triaxial tests (Table 6) was calculated according to the following formula:

$$W_p = \int p d\varepsilon_v^p + q d\varepsilon_s^p \quad (2)$$

where  $p$  = mean effective stress;  $q$  = deviatoric stress;  $\varepsilon_v^p$  = plastic volumetric strain; and  $\varepsilon_s^p$  = plastic shear strain. Fig. 12 shows the



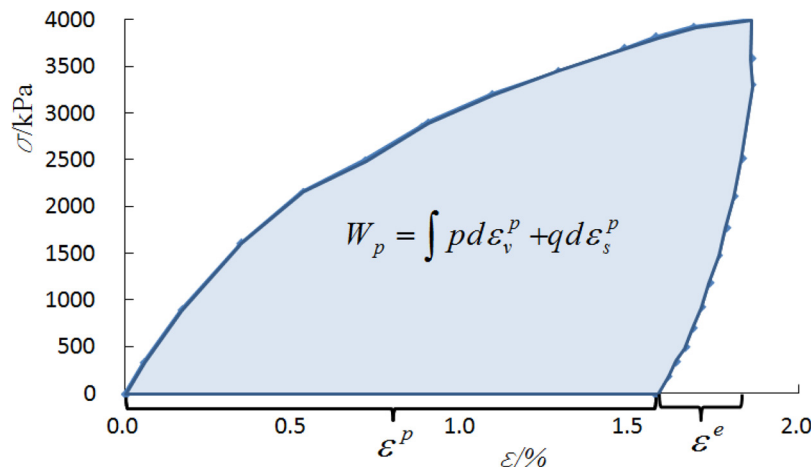


Fig. 12. (Color)  $W_p$  calculated using the stress-strain curve

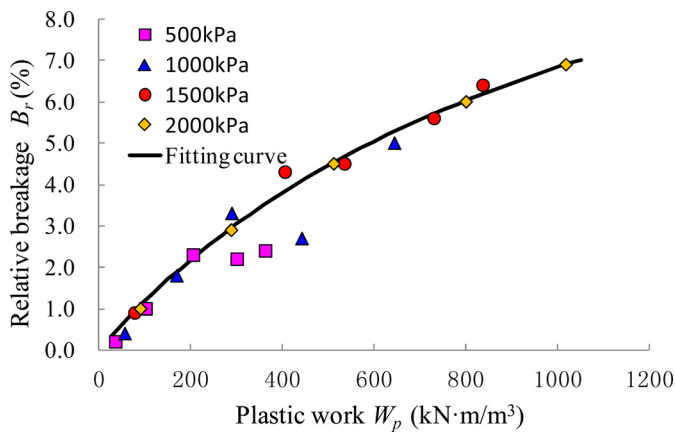


Fig. 13. (Color)  $B_r$  related to plastic work  $W_p$

procedure used to calculate  $W_p$  with the triaxial stress-strain curve of the Gushui basalt rockfill. Table 5 lists the  $\epsilon_s^p$ ,  $\epsilon_v^p$ , and  $W_p$  values during the triaxial test at a confining pressure of 2,000 kPa.

Fig. 13 shows the relationship between  $B_r$  and  $W_p$ . According to monotonic tests and cyclic triaxial tests of the Zipingpu CFRD rockfill, Liu et al. (2014) proposed that the relationship between  $B_r$  (after tests) and  $W_p$  could be simulated by using the following hyperbolic formulation:

$$B_r = \frac{W_p}{A + B \cdot W_p} \quad (3)$$

where  $A$  and  $B$  = fitting parameters.

The fitting curve calculated with Eq. (3) is also plotted in Fig. 13, in which  $A = 7816$  and  $B = 6.8$ . Most of the  $B_r$  values could be accurately simulated by Eq. (3), with the exception of the two points at a confining pressure of 500 kPa, which exhibited a large dilatancy. The large dilatancy decreased the  $W_p$  consumed by the particle breakage. Thus, the  $B_r$  value calculated according to Eq. (3) was larger than the test values.

## Conclusions

In this paper, a series of triaxial tests that used the basalt rockfill of the Gushui CFRD were performed to investigate the rockfill particle

breakage during triaxial tests. The main conclusions are summarized as follows:

1. The particle breakage of the Gushui basalt rockfill from hammer compaction during specimen preparation was highly significant (approximately 0.45–1.29 times the particle breakage generated during shearing), particularly at a high dry density (higher than 2.0 g/cm<sup>3</sup>); thus, this breakage could not be ignored compared with the particle breakage during shearing.
2. Compared with the particle breakage of the Gushui basalt rockfill that occurred during specimen preparation, negligible particle breakage occurred during isotropic consolidation, even at a confining pressure of 1,500 kPa.
3. Under a low confining pressure (100 kPa), the particle sliding and roll over in the Gushui basalt rockfill were loosely constrained; the contact force among the particles was small, and negligible particle breakage occurred during triaxial shearing. Additionally, significant dilatancy occurred, and the deviator stress was generated by the sliding friction and dilatancy. Under a high confining pressure (greater than 500 kPa), the particle sliding and roll over in the Gushui basalt rockfill were more constrained, the contact force significantly increased, and significant particle breakage occurred, which increased with increasing shear strain.
4. During the triaxial shearing, Gushui basalt particles with larger diameters broke first, whereas smaller diameter Gushui basalt particles began breaking with increasing confining pressure. The percentage of particles with diameters under 0.25 mm consistently increased with increasing shearing strain, and the amplitude increased with increasing confining pressure.
5. The relative breakage  $B_r$  during the shearing in the triaxial test was affected by both the shear strain and stress. The relationship between  $B_r$  and the plastic work  $W_p$  could be simulated by using a hyperbolic formulation.
6. As Fig. 11 shows, no particle breakage occurred for some shear strain values (marked as  $\epsilon_{si}$ ) at the beginning of the CD triaxial compression test. Within this initial shear strain  $\epsilon_{si}$ , all the basalt rockfill particles remained in an elastic-plastic state, and the rockfill shear strain consisted of elastic deformation, plastic deformation, sliding, and rolling over. In this test,  $\epsilon_{si}$  increased with decreasing confining pressure. Once the confining pressure was not sufficiently large to limit particle roll over (such as less than 100 kPa in this research),  $\epsilon_{si}$  would cover the entire set of shear strain values, and no obvious particle breakage occurred in the test.

7. The rockfill material did not exhibit a stable critical state friction angle, which differs from sand and clay. Under a low confining pressure (such as 100 kPa in this research), the particles on the sliding plane in the soil constantly rolled over and slid, which complicated the structure of the sliding plane and constantly changed the friction angle. Under a high confining pressure, the particle breakage constantly changed the gradation of the particles on the sliding plane, which also changed the friction angle.

Moreover, particle breakage in the rockfill material was also influenced by other factors, such as the particle shape, fractures and joints in the particles, particle material, stress path of loading, wetting, and so forth, which determined the  $\varepsilon_{si}$  value and the parameters in Eq. (3). Particle crushing tests, complex stress path tests, and wetting tests will be performed to investigate the effects of these factors and will be published in subsequent papers.

## Acknowledgments

This research was supported by the National Natural Science Foundation of China (Grants 51421064, 51379029, 51576029, 51109027, and 51179024).

## Notation

The following symbols are used in this paper:

- $A$  = fitting parameter;
- $B$  = fitting parameter;
- $B_p$  = breakage potential  $B_p$ ;
- $B_r$  = relative breakage factor;
- $B_t$  = total breakage factor;
- $e_i$  = initial void ratio;
- $h$  = scratch hardness;
- $n_b$  = breakage number;
- $n_s$  = shape number;
- $P_a$  = atmospheric pressure;
- $p$  = mean effective stress;
- $q$  = deviatoric stress;
- $W_p$  = plastic work;
- $\varepsilon^p$  = plastic strain;
- $\varepsilon_s^p$  = plastic shear strain;
- $\varepsilon_v^p$  = plastic volumetric strain;
- $\varepsilon_s$  = shear strain;
- $\varepsilon_v$  = volumetric strain;
- $\sigma = p$  or  $q$ ;
- $\sigma_b$  = breakage effective stress;
- $\sigma_r$  = breakage reference stress;
- $\sigma_0$  = effective octahedral normal stresses;
- $\sigma_1$  = major principal stress;
- $\sigma_3$  = minor principal stress;
- $(\sigma_1 - \sigma_3)_{\max}$  = maximum  $(\sigma_1 - \sigma_3)$  before unloading; and
- $\tau_0$  = effective octahedral shear stresses.

## References

- Chavez, C., and Alonso, E. E. (2003). "A constitutive model for crushed granular aggregates which includes suction effects." *Soils Found.*, 43(4), 215–227.
- CS (Chinese Standard). (1999). "Standard test methods for soils." *SL237-1999*, China Water Conservancy and Hydropower Press, Beijing.
- Cooper, W. L., and Breaux, B. A. (2010). "Grain fracture in rapid particulate media deformation n and a particulate media research roadmap from the PMEE workshops." *Int. J. Fract.*, 162(1–2), 137–150.

- Gao, Y., Zhang, B., Liu, W., and Ai, Y. (2009). "Experimental study on particle breakage behavior of rockfills in large-scale triaxial tests." *Yantu Lixue/Rock Soil Mech.*, 30(5), 1237–1240.
- Griffith, A. A. (1921). "The phenomena of rupture and flow in solids." *Philos. Trans. R. Soc. London, Ser. A*, 221(582–593), 163–198.
- Hardin, B. (1985). "Crushing of soil particles." *J. Geotech. Eng.*, 10.1061/(ASCE)0733-9410(1985)111:10(1177), 1177–1192.
- Indraratna, B., Ngo, N., and Rujikiatkamjorn, C. (2013). "Deformation of coal fouled ballast stabilized with geogrid under cyclic load." *J. Geotech. Geoenviron. Eng.*, 10.1061/(ASCE)GT.1943-5606.0000864, 1275–1289.
- Indraratna, B., Ngo, N., Rujikiatkamjorn, C., and Vinod, J. S. (2014). "Behavior of fresh and fouled railway ballast subjected to direct shear testing: Discrete element simulation." *Int. J. Geomech.*, 10.1061/(ASCE)GM.1943-5622.0000264, 34–44.
- Indraratna, B., and Salim, W. (2002). "Modelling of particle breakage of coarse aggregates incorporating strength and dilatancy." *Proc. Inst. Civ. Eng. Geotech. Eng.*, 155(4), 243–252.
- Indraratna, B., Thakur, P., and Vinod, J. (2010). "Experimental and numerical study of railway ballast behavior under cyclic loading." *Int. J. Geomech.*, 10.1061/(ASCE)GM.1943-5622.0000055, 136–144.
- Indraratna, B., Thakur, P., Vinod, J., and Salim, W. (2012). "Semiempirical cyclic densification model for ballast incorporating particle breakage." *Int. J. Geomech.*, 10.1061/(ASCE)GM.1943-5622.0000135, 260–271.
- Jensen, R., Plesha, M., Edil, T., Bosscher, P., and Kahla, N. (2001). "DEM simulation of particle damage in granular media—Structure interfaces." *Int. J. Geomech.*, 10.1061/(ASCE)1532-3641(2001)1:1(21), 21–39.
- Jia, Y.-F., Chi, S.-C., Yang, J., and Lin, G. (2009). "Measurement of breakage energy of coarse granular aggregates." *Yantu Lixue/Rock Soil Mech.*, 30(7), 1960–1966.
- Kong, X., Liu, J., Zou, D., and Liu, H. (2016). "Stress-dilatancy relationship of Zipingpu gravel under cyclic loading in triaxial stress states." *Int. J. Geomech.*, 10.1061/(ASCE)GM.1943-5622.0000584, 04016001.
- Kong, X.-J., Zhou, Y., Xu, B., and Zou, D.-G. (2010). "Analysis on seismic failure mechanism of Zipingpu dam and several reflections of aseismic design for high rock-fill dam." *Proc., 12th Int. Conf. on Engineering, Science, Construction, and Operations in Challenging Environments-Earth and Space 2010*, ASCE, Reston, VA, 3177–3189.
- Li, X., Wang, Z., Liang, Y., and Duan, Q. (2016). "Mixed FEM-crushable DEM nested scheme in second-order computational homogenization for granular materials." *Int. J. Geomech.*, 10.1061/(ASCE)GM.1943-5622.0000627, C4016004.
- Liu, H., Zou, D., and Liu, J. (2014). "Constitutive modeling of dense gravelly soils subjected to cyclic loading." *Int. J. Numer. Anal. Methods Geomech.*, 38(14), 1503–1518.
- Lobo-Guerrero, S., Vallejo, L., and Vesga, L. (2006). "Visualization of crushing evolution in granular materials under compression using DEM." *Int. J. Geomech.*, 10.1061/(ASCE)1532-3641(2006)6:3(195), 195–200.
- Ma, H., and Cao, K. (2007). "Key technical problems of extra-high concrete faced rock-fill dam." *Sci. China Ser. E: Technol. Sci.*, 50(S1), 20–33.
- Marachi, N. D., Chan, C. K., and Seed, H. B. (1972). "Evaluation of properties of rockfill materials." *J. Soil Mech. Found. Div.*, 98(SM1), 95–114.
- Marsal, R. J. (1967). "Large scale testing of rockfill materials." *J. Soil Mech. Found. Div.*, 27–43.
- McDowell, G. R. (2003). "Micromechanics of creep of granular materials." *Géotechnique*, 53(10), 915–916.
- McDowell, G. R., and Bolton, M. D. (1998). "On the micromechanics of crushable aggregates." *Géotechnique*, 48(5), 667–679.
- Oldecop, L. A., and Alonso, E. E. (2001). "A model for rockfill compressibility." *Géotechnique*, 51(2), 127–139.
- Salim, W., and Indraratna, B. (2004). "A new elastoplastic constitutive model for coarse granular aggregates incorporating particle breakage." *Can. Geotech. J.*, 41(4), 657–671.
- Sun, Q. D., Indraratna, B., and Nimbalkar, S. (2014). "Effect of cyclic loading frequency on the permanent deformation and degradation of railway ballast." *Géotechnique*, 64(9), 746–751.

- Varadarajan, A., Sharma, K., Abbas, S., and Dhawan, A. (2006). "Constitutive model for rockfill materials and determination of material constants." *Int. J. Geomech.*, [10.1061/\(ASCE\)1532-3641\(2006\)6:4\(226\)](#), 226–237.
- Wu, Y., Zhang, B., Yu, Y., and Zhang, Z. (2016). "Consolidation analysis of Nuozhadu high earth-rockfill dam based on the coupling of seepage and stress-deformation physical state." *Int. J. Geomech.*, [10.1061/\(ASCE\)GM.1943-5622.0000555](#), 04015085.
- Xiao, Y., Coop, M. R., Liu, H., Liu, H., and Jiang, J. (2016a). "Transitional behaviors in well-graded coarse granular soils." *J. Geotech. Geoenviron. Eng.*, [10.1061/\(ASCE\)GT.1943-5606.0001551](#), 06016018.
- Xiao, Y., and Liu, H. (2017). "Elastoplastic constitutive model for rockfill materials considering particle breakage." *Int. J. Geomech.*, [10.1061/\(ASCE\)GM.1943-5622.0000681](#), 04016041.
- Xiao, Y., Liu, H., Chen, Y., and Jiang, J. (2014). "Strength and deformation of rockfill material based on large-scale triaxial compression tests. II: Influence of particle breakage." *J. Geotech. Geoenviron. Eng.*, [10.1061/\(ASCE\)GT.1943-5606.0001177](#), 04014071.
- Xiao, Y., Liu, H., Desai, C., Sun, Y., and Liu, H. (2016b). "Effect of intermediate principal-stress ratio on particle breakage of rockfill material." *J. Geotech. Geoenviron. Eng.*, [10.1061/\(ASCE\)GT.1943-5606.0001433](#), 06015017.
- Xiao, Y., Liu, H., Xiao, P., and Xiang, J. (2016c). "Fractal crushing of carbonate sands under impact loading." *Géotechnique Lett.*, [6\(3\)](#), 199–204.
- Xiao, Y., Liu, H., Zhang, W., Liu, H., Yin, F., and Wang, Y. (2016d). "Testing and modeling of rockfill materials: A review." *J. Rock Mech. Geotech. Eng.*, [8\(3\)](#), 415–522.
- Xiao, Y., Sun, Y., and Hanif, K. F. (2015). "A particle-breakage critical state model for rockfill material." *Sci. China Ser. E: Technol. Sci.*, [58\(7\)](#), 1125–1136.
- Yang, G., Zhang, B.-Y., Yu, Y.-Z., and Sun, X. (2010). "An experimental study on particle breakage of coarse-grained materials under various stress paths." *Shuili Xuebao/J. Hydraul. Eng.*, [41\(3\)](#), 338–342.
- Zhang, B., Jie, Y., and Kong, D.-Z. (2014). "Particle breakage of cement ellipsoid aggregate-Part I: Triaxial compression tests." *J. Test. Eval.*, [42\(1\)](#), 1–11.
- Zhang, B. Y., Zhang, J. H., and Sun, G. L. (2012). "Particle breakage of argillaceous siltstone subjected to stresses and weathering." *Eng. Geol.*, [137–138](#), 21–28.
- Zhang, B. Y., Zhang, J. H., and Sun, G. L. (2015). "Deformation and shear strength of rockfill materials composed of soft siltstones subjected to stress, cyclical drying/wetting and temperature variations." *Eng. Geol.*, [190](#), 87–97.